Single-Molecule Continuous-Wave Terahertz Rectification Spectroscopy and Microscopy

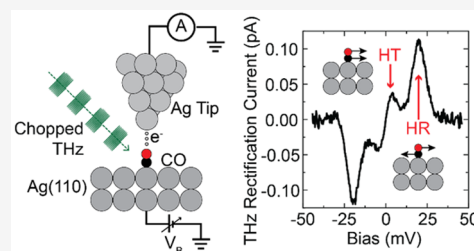Siyu Chen, Wenlu Shi, and W. Ho*

ACCESS | Metrics & More | Article Recommendations | Supporting Information

ABSTRACT: We report rectification spectroscopy (RS) for single molecules performed with continuous-wave terahertz (CW THz) radiation at the tunneling junction of a scanning tunneling microscope (STM) at 8 K. CW THz-RS serves as a new technique in single-molecule vibrational and magnetic excitation spectroscopy besides inelastic electron tunneling spectroscopy (IETS). By quantitatively studying IETS and THz RS, we show that CW THz induces a sinusoidal bias modulation with amplitude linearly dependent on the THz far-field amplitude. Such THz-induced bias modulation amplitude appears to be sensitive to the THz beam alignment but insensitive to variation in the tunneling gap far smaller than the THz wavelength.

KEYWORDS: scanning tunneling microscope, continuous-wave terahertz wave, rectification spectroscopy, inelastic electron tunneling spectroscopy, single-molecule spectroscopy

Rectifiers such as semiconductor and vacuum tube diodes are widely used in power electronics to convert AC into DC signals. In the context of a single molecule in a tunneling junction, nonlinearity in the $I-V$ curve, associated with inelastic electron tunneling, gives rise to rectification current from an AC bias modulation. Indeed, experiments have demonstrated atomic-scale rectification by coupling 800 MHz microwave radiation into a tunneling junction.[1,2] However, single-molecule RS performed with a continuous-wave (CW) THz source[3−5] has not been reported. While a signal generator provides the microwave voltage bias modulation through a coaxial cable, laser radiation freely propagating in space delivers the THz electric field oscillations into the STM junction. On the other hand, although laser-induced rectification was previously observed by coupling mid-infrared radiation into a tunneling junction,[6] such a measurement typically requires high laser intensity and small tunneling gap to achieve a good signal-to-noise ratio. Such requirements lead to an unstable tunneling gap due to laser-induced thermal expansion and molecular mobility or reaction, and make it unsuitable for single-molecule spectroscopy. Here, the CW THz-RS technique provides a nondestructive approach for light-induced single-molecule spectroscopy in addition to IETS measurement.

Coupling ultrafast THz pulses[7−10] into an STM junction generates transient voltage pulses[11,12] that can induce nano-scale ultrafast dynamics.[13−20] However, the voltage pulses in the tunneling junction often have a high peak intensity of up to several volts and are too strong for low-energy spectroscopy of single molecules. Moreover, obtaining high energy resolution in THz time domain spectroscopy (TDS) requires an extended 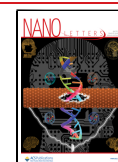delay scan range, which can be very time-consuming in application.[21,22] Therefore, it is desirable to incorporate THz frequency domain spectroscopy (FDS) as a new approach for single-molecule spectroscopy. With the chemical and spatial sensitivity demonstrated for microwave RS, it is promising to implement CW THz rectification for single-molecule FDS by extending to the higher THz frequency range that is not covered by IETS[23−25] and electron spin resonance spectroscopy.[26]

In this study, we demonstrated CW THz-RS for five different single-molecule species and two different substrates, extending the rectifying source frequency to the THz gap. We also quantitatively investigated the near-field voltage across the tunneling junction induced by THz radiation and the influence of its far-field intensity on the line shape and signal intensity for CW THz-RS. Figure 1a shows the experimental setup for CW THz-STM. The THz radiation was generated from a photoconductive antenna (PCA) emitter and directly focused into the STM junction. The THz field intensity is controlled by the voltage supplied to the PCA emitter (V_{PCA}). A square wave V_{PCA} chopped the THz radiation and induced a periodic change in tunneling current (Figure 1b). The THz-induced rectification current was measured by extracting the first-harmonic component from the STM tunneling current through lock-in detection. Recording the rectification current as a
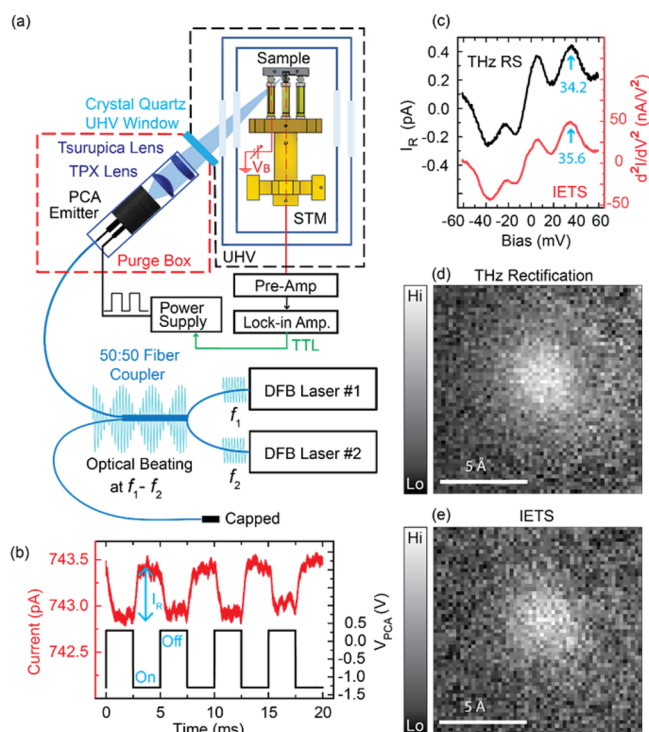
Figure 1. Single-molecule CW THz rectification spectroscopy (THz-RS) with an 8-K STM. (a) Schematic diagram of the experimental setup for CW THz-STM. The continuous-wave THz is generated through an optical heterodyning process with an InGaAs photoconductive antenna (PCA) emitter (Toptica TeraScan1550). Two tunable distributed feedback (DFB) lasers form an optical beating at their frequency difference and drive the THz radiation at the PCA emitter. The THz beam with p-polarization is collimated by a TPX lens (BaTOP GmbH) and focused by a Tsurupica lens (Broadband Inc.) into the STM junction at a 45° angle from the tip axis. The PCA emitter and lenses are mounted in a lens tube assembly and enclosed in a N_2-purge box attached outside of the UHV chamber. The THz field amplitude is controlled by the voltage supplied to the PCA emitter. (b) Tunneling current (red, showing the rectification component) and control voltage of the PCA emitter (V_{PCA}, −1.3 to +0.3 V square wave, black) measured simultaneously with the tip over the center of a CO molecule adsorbed on a Cu(001) surface at 8 K. The input THz radiation was set to 0.400 THz and chopped by a 200 Hz square wave. Feedback was turned off at a tunneling gap set point of −60 mV/1 nA, and the sample−tip bias was set to +35.6 mV (CO hindered rotation peak) for the measurement. The tunneling current was averaged 4096 passes to obtain a good signal-to-noise ratio. (c) THz rectification spectrum (black) and IETS spectrum (red) obtained over the same CO molecule, at the same set point (−60 mV/1 nA). (d) THz rectification imaging over the same CO molecule, obtained at a bias of +34.2 mV with 0.400 THz radiation chopped at 273 Hz. (e) IETS imaging over the same CO molecule, obtained at a bias of +35.6 mV with 273 Hz sinusoidal bias modulation. Both (d) and (e) were acquired at the same set point (−60 mV/0.8 nA), and the imaging biases are indicated in (c) with blue arrows.

function of the DC tip−substrate bias with a fixed tip height generated a THz-RS spectrum. Here, by comparing the THz-RS to IETS in both spectroscopy (Figure 1c) and imaging (Figure 1d,e) for a carbon monoxide (CO) molecule, we observed chemical sensitivity and spatial resolution for these two types of measurement.

To understand how THz far-field radiation coupled to the STM junction, we measured IETS spectra over CO on an

Ag(110) surface with nonchopped THz radiation (Figure 2a). THz field intensity was controlled by tuning the DC voltage supplied to the PCA emitter ($V_{PCA,C}$). Under the influence of
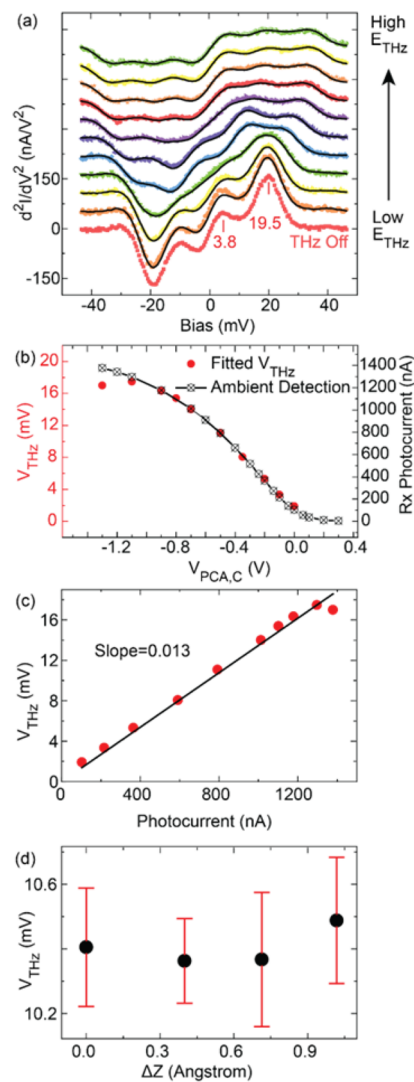

Figure 2. Inelastic electron tunneling spectroscopy (IETS) obtained with nonchopped THz irradiation. (a) IETS of CO adsorbed on an Ag(110) surface taken without THz and with nonchopped 0.150 THz radiation of different far-field amplitudes (E_{THz}). E_{THz} was tuned by $V_{PCA,C}$. For each value of $V_{PCA,C}$, the measured data (colored dots) and fitting results (black solid curves) are offset for clarity. All IETS spectra were taken with a tunneling set point of 40 mV/0.8 nA and a bias modulation of 273 Hz and 3 mV RMS amplitude sinusoidal wave. No shift in HT and HR mode energies is resolved for the THz-free IETS spectra and IETS spectra obtained with the lowest three $V_{PCA,C}$ values. (b) THz-induced voltage across a tip−substrate junction obtained from fitting results in (a) (V_{THz}, red circles) and the THz photocurrent measured by PCA receiver (Rx photocurrent, black boxed crosses) using ambient detection as a function of $V_{PCA,C}$. (c) V_{THz} as a function of Rx photocurrent (red circles) and a linear fit between the two variables (black line). (d) V_{THz} as a function of change in tip−substrate gap ΔZ, with $\Delta Z = 0$ being defined for the tunneling set point of 40 mV/2 nA with the tip over the center of CO. For each tip−substrate gap, an IETS spectrum with nonchopped THz radiation at 0.150 THz and $V_{PCA,C}$ = −0.35 V was measured and fitted to obtain V_{THz}. Error bars indicate 95% confidence intervals for the fitting results. No significant variation in V_{THz} is observed within the range of tunneling gap used.

THz-induced near-field radiation in the junction, we observed increasing peak splitting in the IETS spectra with increasing THz far-field amplitude that is consistent with a bias redistribution under THz irradiation. Assuming CW THz radiation induced a sinusoidal bias modulation in the junction with the amplitude V_{THz}, the IETS spectral waveform is mathematically expressed as a convolution between an IETS spectrum in the absence of THz illumination and a probability weight function of the THz-induced bias modulation:[2,27]

$$S_{on}(V_0, V_{THz}) = \int_{V_0 - V_{THz}}^{V_0 + V_{THz}} S_{off}(V) w(V, V_0, V_{THz}) \, dV \tag{1}$$

Here, V_0 is the DC bias across the tunneling junction, $S_{off}(V)$ is the THz-free IETS waveform, and $w(V, V_0, V_{THz})$ is the weight function representing the normalized probability distribution of the THz-induced voltage. The weight function for a sinusoidal bias modulation is written as

$$w(V, V_0, V_{THz}) = \frac{1}{\pi\sqrt{V_{THz}^2 - (V - V_0)^2}} \quad |V - V_0| < V_{THz} \tag{2}$$

Fitting each IETS spectrum in Figure 2a according to eqs 1 and 2, we obtained V_{THz} as a function of $V_{PCA,C}$ (Figure 2b). The fitted V_{THz} follows a trend similar to that of the THz photocurrent detected by the PCA receiver (Rx photocurrent) using ambient detection as a function of the $V_{PCA,C}$ used for THz generation (see section III in the Supporting Information for details of the ambient detection method). Plotting fitted V_{THz} against Rx photocurrent, we obtained a linear relation between the two variables with a slope of 0.013 mV/nA (Figure 2c). Since the Rx photocurrent is proportional to the THz far-field amplitude E_{THz}, we can claim that V_{THz} is linearly proportional to E_{THz}, with the slope indicating the relative near-field enhancement in the STM junction.

Using this calibration method, we measured V_{THz} induced by nonchopped 0.150 THz radiation at different tip−substrate distances (Figure 2d) and found it to be nearly constant within the measured range of tunneling gap. When the tip−substrate distance is far smaller than the THz wavelength, field retardation is negligible and the THz quasi-static near-field in the junction can lead to constant amplitude in the THz-induced voltage in the STM junction.[28] The tip−substrate gap range used for measurement is estimated to be from 3.2 to 4.2 Å (see details for the estimation of tunneling gap in section IV in the Supporting Information). Therefore, the quasi-static approximation is valid for the full range of THz frequency (0.050−1.290 THz) provided by our experimental setup, with a wavelength of ∼2 mm at 0.150 THz.

To further investigate how THz field intensity affects the rectification signal, we measured THz-RS spectra of the same CO molecule with different THz far-field amplitude E_{THz} (Figure 3a). We resolved both hindered translation (HT) and hindered rotation (HR) modes for CO from the spectra at low E_{THz} and observed a significant peak broadening with increasing E_{THz} (see section VI in the Supporting Information for a detailed discussion of peak broadening). We further extracted V_{THz} by numerically fitting each THz-RS spectrum with the THz-free IETS spectrum obtained at the same tunneling set point and tip position (see details of the fitting process in section V in the Supporting Information). The fitted THz-RS curves closely follow measured data, and the fitted V_{THz} values vary as the Rx photocurrent on the PCA voltage
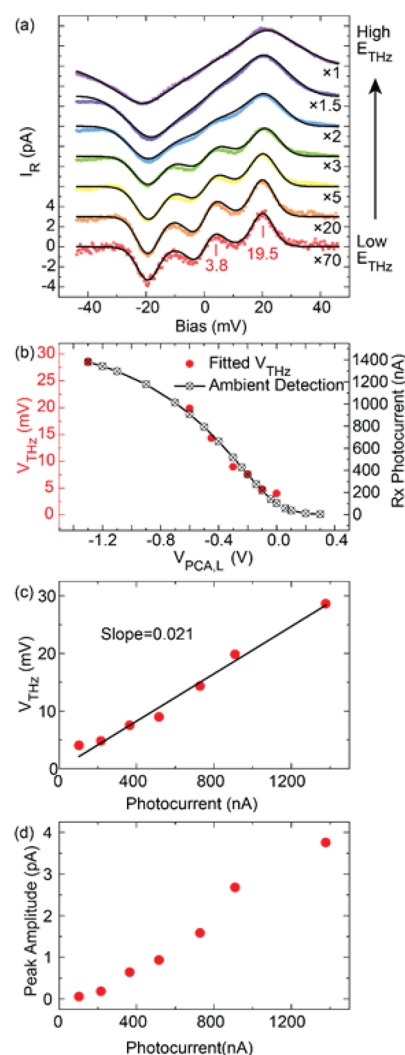

Figure 3. THz-RS with different THz far-field intensities. (a) THz rectification spectra for a single CO adsorbed on an Ag(110) surface obtained with THz radiation at different far-field intensities (E_{THz}). The THz radiation was set to 0.150 THz and chopped at 273 Hz by supplying the PCA emitter with a square wave that alternated between a fixed high level +0.3 V (THz off) and a variable low level ($V_{PCA,L}$, THz on). For each value of $V_{PCA,L}$, both experimental data (colored dots) and corresponding fitting results (black curves) are scaled and offset for clarity. All THz rectification spectra displayed here are background subtracted for better line shape analysis (see details of background subtraction in section IX in the Supporting Information). No shift in HT and HR mode energies is resolved from the spectra obtained using the lowest four $V_{PCA,L}$ values. (b) THz-induced voltage across the tip−substrate junction (V_{THz}, red circles) obtained from fitting results in (a) and THz photocurrent measured by the PCA receiver (Rx photocurrent, black boxes with cross) as a function of $V_{PCA,L}$, obtained by ambient detection (see details of the method in section III in the Supporting Information). (c) V_{THz} as a function of Rx photocurrent (red circles) and the linear fit between the two variables (black line). (d) Peak amplitude of CO hindered rotation (HR) mode (19.5 meV) as a function of Rx photocurrent.

used for THz generation (Figure 3b). The linear fit of V_{THz} against Rx photocurrent yields a slope larger than that presented in Figure 2c, indicating a greater near-field enhancement in the junction likely due to the different THz beam alignment for THz-RS (Figure 3c).
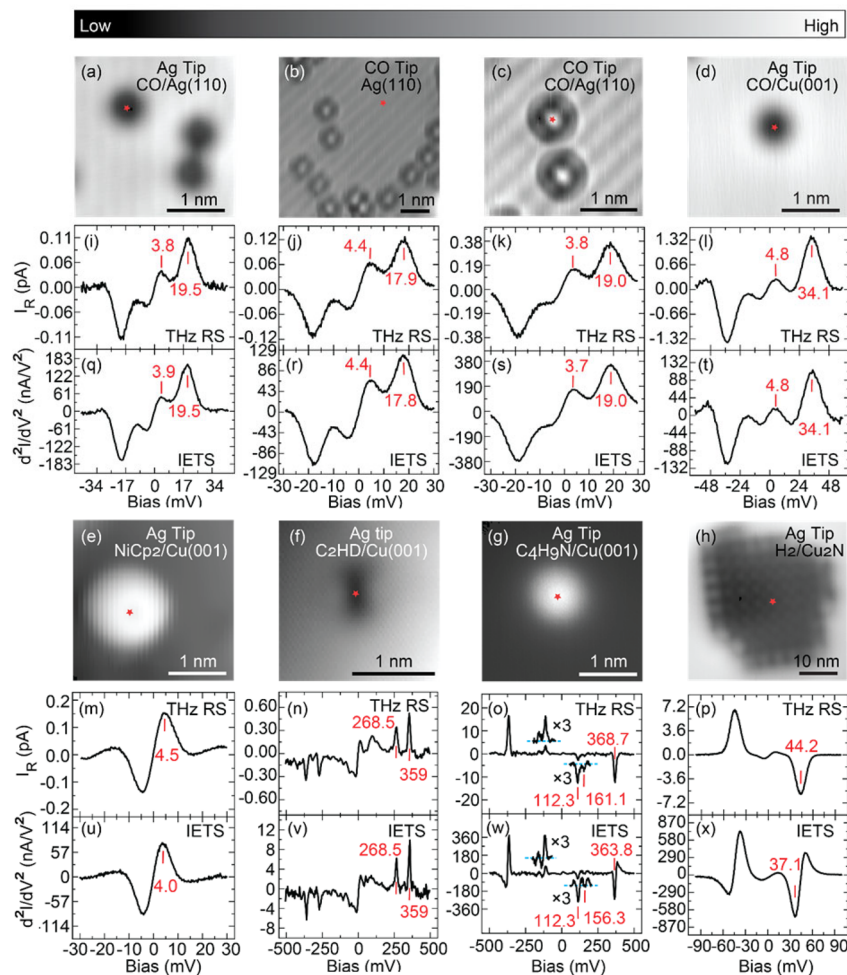
Figure 4. THz rectification spectroscopy (RS) and inelastic electron tunneling spectroscopy (IETS) for various molecules. (a−h) Constant-current topographies of different tip/molecule/substrate systems with red stars (★) indicating the tip position selected for spectral acquisition near the center of each molecular image. The corresponding THz-RS spectra ((i−p)) and IETS spectra ((q−x)) are displayed below each topography. The spectra shown in (i), (q), (l), (t), (n), and (v) were background subtracted to remove features from the metal substrate (see section IX in the Supporting Information). For THz-RS spectra, a square wave chopping frequency of 273 Hz was used for (i−o) and 255.11 Hz for (p); for each corresponding IETS, we applied a sinusoidal bias modulation of the same frequency used for THz chopping in RS. All spectra were measured with a 100 ms lock-in time constant. Other measurement conditions used for topography imaging, THz-RS, and IETS are given in Table S1.

The THz rectification intensity for the CO HR peak increases monotonically with the THz intensity (Figure 3d). Simulation of the HR peak signal as a function of V_{THz} indicates a quadratic dependence for small values of V_{THz} (i.e., <5 mV), accounting for the nonlinear trend as the Rx photocurrent approaches zero (see details of the simulation in section VII in the Supporting Information). Such sensitivity of a molecular vibration on THz far-field intensity suggests a promising application in single-molecule THz sensing through rectification measurement.

Figure 4 displays THz RS spectra and IETS spectra of various molecular species on different metal substrates. For different tip−substrate configurations (Figure 4a−d), THz-RS spectra (Figure 4i−l) obtained at 0.400 THz and the corresponding IETS spectra (Figure 4q−t) exhibited almost identical line shapes and peak positions for CO HR and HT modes. Similar results were obtained for a nickelocene (NiCp$_2$) molecule (Figure 4m,u) and a monodeuterated acetylene (C$_2$HD) molecule (Figure 4n,v) on Cu(001). On the other hand, we found that THz-RS spectral line shapes deviated from the corresponding IETS spectra for pyrrolidine

(C$_4$H$_9$N) and hydrogen (H$_2$) (Figure 4o,w,p,x). While all peaks in the THz-RS spectra showed a symmetrical profile, the peaks in IETS spectra appeared as an asymmetrical peak-dip shape. Rectification spectra obtained with chopped sinusoidal bias modulation showed that the peak profile gradually evolved from asymmetrical to symmetrical line shapes as the modulation frequency increased from 10 kHz to 1 MHz, while no significant changes in line shape were observed for modulation frequencies above 1 MHz (see details in section VIII in the Supporting Information). This suggests that the line shape differences between THz-RS and IETS are likely due to the frequency response of the bias modulation in the sub-MHz range, instead of the resonant excitation in the THz frequency range.

We can qualitatively understand such frequency-dependent line shape changes with the following analysis. Both pyrrolidine and hydrogen in a tunneling junction exhibit two-level conductance switching.[29,30] The potential energy along the switching coordinate can be modeled as an asymmetric double-well potential. When the bias modulation frequency is higher than the switching rate from one state to the other, the

probability of the corresponding switching process will be suppressed. Because of the asymmetry of the double-well potential, increasing the modulation frequency can gradually shift the state population of the molecule toward one of the conductance states, changing the total conductance and therefore the line shape of the rectification spectra. Such a line shape change saturates when the modulation frequency far exceeds the switching rates in both directions, which explains the similar line shapes between THz-RS and MHz-RS. The frequency-dependent change in rectification signal suggests its high sensitivity to the dynamic response of switching systems. Therefore, the THz-induced fast oscillating near field in the tunneling junction can be potentially used to study the atomic-scale switching dynamics in the sub-THz frequency range.

In conclusion, CW THz radiation can induce an effective sinusoidal bias modulation in the STM junction and generate a rectification current that reveals the $I-V$ nonlinearity of the junction. The THz-induced bias modulation amplitude is proportional to its far-field amplitude and sensitive to the THz beam alignment to the STM junction but insensitive to tip−substrate gap variation within the regime of quasi-static approximation. Our results demonstrate the sensitivity of THz rectification to THz power, inelastic electron tunneling-induced molecular excitations, and molecular dynamics.

■ ASSOCIATED CONTENT

ⓈⒾ Supporting Information

The Supporting Information is available free of charge at https://pubs.acs.org/doi/10.1021/acs.nanolett.3c00271.

> Tip and sample preparation, focusing and aligning a THz beam into an STM junction, ambient detection of THz field, estimation of tip−substrate gap, fitting THz-RS based on THz-free IETS, THz-induced peak broadening in rectification spectra, simulation of THz-RS peak amplitude as a function of V_{THz}, low-frequency AC rectification spectra for hydrogen and pyrrolidine, and background subtraction of spectra (PDF)

■ AUTHOR INFORMATION

Corresponding Author

W. Ho − *Department of Physics and Astronomy, University of California, Irvine, California 92697-4575, United States; Department of Chemistry, University of California, Irvine, California 92697-2025, United States;* ⓞ orcid.org/0000-0003-3884-2142; Email: wilsonho@uci.edu

Authors

Siyu Chen − *Department of Physics and Astronomy, University of California, Irvine, California 92697-4575, United States;* ⓞ orcid.org/0009-0002-6712-8300

Wenlu Shi − *Department of Physics and Astronomy, University of California, Irvine, California 92697-4575, United States;* ⓞ orcid.org/0000-0001-6103-5694

Complete contact information is available at:
https://pubs.acs.org/10.1021/acs.nanolett.3c00271

Notes

The authors declare no competing financial interest.

■ ACKNOWLEDGMENTS

■ REFERENCES

(1) Lee, J.; Tu, X.; Ho, W. Spectroscopy and Microscopy of Spin-Sensitive Rectification Current. *Nano Lett.* **2005**, *5* (12), 2613−2617.

(2) Tu, X.; Lee, J.; Ho, W. Atomic-Scale Rectification at Microwave Frequency. *J. Chem. Phys.* **2006**, *124* (2), 021105.

(3) Matsuura, S.; Tani, M.; Sakai, K. Generation of Coherent Terahertz Radiation by Photomixing in Dipole Photoconductive Antennas. *Appl. Phys. Lett.* **1997**, *70* (5), 559−561.

(4) Moumane, I.; Zbitou, J.; Latrach, M.; Errkik, A.; Chakkor, O.; Fouad, A. Design of CW THz Photonic Transmitter Based on Low Pass-Filter and Bow-Tie Wideband Antenna. *Int. J. Electr. Comput.* **2018**, *8* (5), 3801−3808.

(5) Liebermeister, L.; Nellen, S.; Kohlhaas, R.; Breuer, S.; Schell, M.; Globisch, B. Ultra-Fast, High-Bandwidth Coherent CW THz Spectrometer for Non-Destructive Testing. *J. Infrared Millim. Terahertz Waves* **2019**, *40* (3), 288−296.

(6) Völcker, M.; Krieger, W.; Walther, H. Laser-Driven Scanning Tunneling Microscope. *Phys. Rev. Lett.* **1991**, *66* (13), 1717−1720.

(7) Siders, C. W.; Siders, J. L. W.; Taylor, A. J.; Park, S.-G.; Melloch, M. R.; Weiner, A. M. Generation and Characterization of Terahertz Pulse Trains from Biased, Large-Aperture Photoconductors. *Opt. Lett.* **1999**, *24* (4), 241−243.

(8) Shen, Y. C.; Upadhya, P. C.; Beere, H. E.; Linfield, E. H.; Davies, A. G.; Gregory, I. S.; Baker, C.; Tribe, W. R.; Evans, M. J. Generation and Detection of Ultrabroadband Terahertz Radiation Using Photoconductive Emitters and Receivers. *Appl. Phys. Lett.* **2004**, *85* (2), 164−166.

(9) Kini, R. N.; Kent, A. J.; Stanton, N. M.; Henini, M. Generation and Detection of Terahertz Coherent Transverse-Polarized Acoustic Phonons by Ultrafast Optical Excitation of GaAs/AlAs Superlattices. *Appl. Phys. Lett.* **2006**, *88* (13), 134112.

(10) Wilke, I.; Sengupta, S. Nonlinear Optical Techniques for Terahertz Pulse Generation and Detection-Optical Rectification and Electrooptic Sampling. In *Terahertz Spectroscopy: Principles and Applications*, 1st ed.; CRC Press: 2007; pp 41−72.

(11) Cocker, T. L.; Jelic, V.; Gupta, M.; Molesky, S. J.; Burgess, J. A. J.; Reyes, G. D. L.; Titova, L. V.; Tsui, Y. Y.; Freeman, M. R.; Hegmann, F. A. An Ultrafast Terahertz Scanning Tunnelling Microscope. *Nat. Photonics* **2013**, *7* (8), 620−625.

(12) Ammerman, S. E.; Wei, Y.; Everett, N.; Jelic, V.; Cocker, T. L. Algorithm for Subcycle Terahertz Scanning Tunneling Spectroscopy. *Phys. Rev. B* **2022**, *105* (11), 115427.

(13) Cocker, T. L.; Peller, D.; Yu, P.; Repp, J.; Huber, R. Tracking the Ultrafast Motion of a Single Molecule by Femtosecond Orbital Imaging. *Nature* **2016**, *539* (7628), 263−267.

(14) Jelic, V.; Iwaszczuk, K.; Nguyen, P. H.; Rathje, C.; Hornig, G. J.; Sharum, H. M.; Hoffman, J. R.; Freeman, M. R.; Hegmann, F. A. Ultrafast Terahertz Control of Extreme Tunnel Currents through Single Atoms on a Silicon Surface. *Nat. Phys.* **2017**, *13* (6), 591−597.

(15) Luo, Y.; Jelic, V.; Chen, G.; Nguyen, P. H.; Liu, Y. J. R.; Calzada, J. A. M.; Mildenberger, D. J.; Hegmann, F. A. Nanoscale Terahertz STM Imaging of a Metal Surface. *Phys. Rev. B* **2020**, *102* (20), 205417.

(16) Lange, S. L.; Noori, N. K.; Kristensen, T. M. B.; Steenberg, K.; Jepsen, P. U. Ultrafast THz-Driven Electron Emission from Metal Metasurfaces. *J. Appl. Phys.* **2020**, *128* (7), 070901.

(17) Cocker, T. L.; Jelic, V.; Hillenbrand, R.; Hegmann, F. A. Nanoscale Terahertz Scanning Probe Microscopy. *Nat. Photonics* **2021**, *15* (8), 558−569.

(18) Yoshida, S.; Arashida, Y.; Hirori, H.; Tachizaki, T.; Taninaka, A.; Ueno, H.; Takeuchi, O.; Shigekawa, H. Terahertz Scanning Tunneling Microscopy for Visualizing Ultrafast Electron Motion in Nanoscale Potential Variations. *ACS Photonics* **2021**, *8* (1), 315−323.

(19) Tachizaki, T.; Hayashi, K.; Kanemitsu, Y.; Hirori, H. On the Progress of Ultrafast Time-Resolved THz Scanning Tunneling Microscopy. *APL Mater.* **2021**, *9* (6), 060903.

(20) Abdo, M.; Sheng, S.; Rolf-Pissarczyk, S.; Arnhold, L.; Burgess, J. A. J.; Isobe, M.; Malavolti, L.; Loth, S. Variable Repetition Rate THz Source for Ultrafast Scanning Tunneling Microscopy. *ACS Photonics* **2021**, *8* (3), 702−708.

(21) Mickan, S. P.; Xu, J.; Munch, J.; Zhang, X.-C.; Abbott, D. The Limit of Spectral Resolution in THz Time-Domain Spectroscopy. *Proc. SPIE* **2004**, *5277*, 54−64.

(22) Wang, L.; Xia, Y.; Ho, W. Atomic-Scale Quantum Sensing Based on the Ultrafast Coherence of an H_2 Molecule in an STM Cavity. *Science* **2022**, *376* (6591), 401−405.

(23) Klein, J.; Léger, A.; Belin, M.; Défourneau, D.; Sangster, M. J. L. Inelastic-Electron-Tunneling Spectroscopy of Metal-Insulator-Metal Junctions. *Phys. Rev. B* **1973**, *7* (6), 2336−2348.

(24) Lambe, J.; Jaklevic, R. C. Molecular Vibration Spectra by Inelastic Electron Tunneling. *Phys. Rev.* **1968**, *165* (3), 821−832.

(25) Stipe, B. C.; Rezaei, M. A.; Ho, W. Single-Molecule Vibrational Spectroscopy and Microscopy. *Science* **1998**, *280* (5370), 1732−1735.

(26) Yang, K.; Paul, W.; Natterer, F. D.; Lado, J. L.; Bae, Y.; Willke, P.; Choi, T.; Ferrón, A.; Fernández-Rossier, J.; Heinrich, A. J.; Lutz, C. P. Tuning the Exchange Bias on a Single Atom from 1 MT to 10 T. *Phys. Rev. Lett.* **2019**, *122* (22), 227203.

(27) Paul, W.; Baumann, S.; Lutz, C. P.; Heinrich, A. J. Generation of Constant-Amplitude Radio-Frequency Sweeps at a Tunnel Junction for Spin Resonance STM. *Rev. Sci. Instrum.* **2016**, *87* (7), 074703.

(28) Müller, M.; Martín Sabanés, N.; Kampfrath, T.; Wolf, M. Phase-Resolved Detection of Ultrabroadband THz Pulses inside a Scanning Tunneling Microscope Junction. *ACS Photonics* **2020**, *7* (8), 2046−2055.

(29) Gaudioso, J.; Lauhon, L. J.; Ho, W. Vibrationally Mediated Negative Differential Resistance in a Single Molecule. *Phys. Rev. Lett.* **2000**, *85* (9), 1918−1921.

(30) Halbritter, A.; Makk, P.; Csonka, S.; Mihály, G. Huge Negative Differential Conductance in Au- H_2 Molecular Nanojunctions. *Phys. Rev. B Condens. Matter* **2008**, *77* (7), 075402.

📖 Recommended by ACS